Adenovirus-Mimetic Nanoparticles: Sequential Ligand–Receptor Interplay as a Universal Tool for Enhanced *In Vitro*/*In Vivo* Cell Identification

Daniel Fleischmann, Sara Maslanka Figueroa, Sebastian Beck, Kathrin Abstiens, Ralph Witzgall, Frank Schweda, Philipp Tauber, and Achim Goepferich*

Cite This: *ACS Appl. Mater. Interfaces* 2020, 12, 34689−34702

Read Online

ACCESS | Metrics & More | Article Recommendations | Supporting Information

ABSTRACT: Viral infection patterns often rely on precisely coordinated sequences of distinct ligand−receptor interactions, leading in many cases to an outstanding target cell specificity. A successful mimicry of viral targeting strategies to create more site-specific nanoparticles (NPs) would therefore require particle−cell interactions to also be adequately controllable. In the present study, hetero-multivalent block-copolymer NPs present their attached ligands in a sterically controlled manner to create a sequential NP−cell interaction similar to the cell infiltration strategy of human adenovirus type 2. Targeting renal mesangial cells, particles therefore initially bind angiotensin II receptor type 1 (AT1r) on the cell surface via a structurally flexible AT1r antagonist. After a mandatory spatial approach, particle endocytosis is realized via binding of immobile $\alpha_V\beta_3$ integrins with a previously concealed secondary ligand, thereby creating a stepwise particle−cell interplay of primary NP attachment and subsequent uptake. Manufactured adenovirus-mimetic NPs show great avidity for both target motifs *in vitro*, leading to a substantial binding as well as subsequent cell uptake into target mesangial cells. Additionally, steric shielding of secondary ligand visibility leads to a highly controllable, sequential ligand−receptor interaction, whereby hetero-functional NPs activate mesangial cell surface integrins only after a successful prior binding to the AT1r. This stepwise cell identification significantly enhances mesangial cell specificity in co-culture assays with different off-target cells. Additionally, described NPs display excellent *in vivo* robustness by efficiently accumulating in the mesangium upon injection, thereby opening new paths for possible drug delivery applications.

Sequential target recognition
Initial attachment — Spatial approach — Endocytosis
Mesangial Cell
In Vitro Selectivity
In Vivo Targeting

KEYWORDS: virus-mimetic nanoparticles, human adenovirus, sequential ligand−receptor interplay, cell-specific targeting, mesangial cells
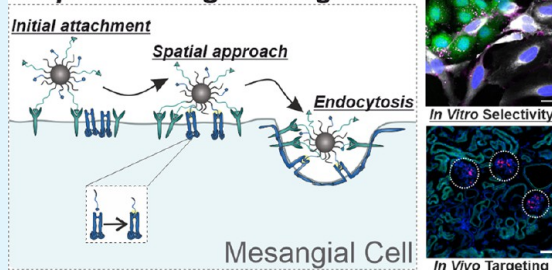
1. INTRODUCTION

Nanomaterials for biomedical applications suffer in many cases from poor availability at the intended site of action.[1−3] A paradigm shift in material design can help overcome poor target cell specificity, which has been identified as one of the main impediments for successful targeting.[4,5] In this context, viruses can serve as a valuable template since they are endowed with the paramount ability to distinguish between off-target and target cells.[6−8] For a successful transfer of this target specificity to novel nanoparticulate approaches, it is crucial to investigate the underlying structural characteristics of viruses and integrate them into the process of nanoparticle (NP) development. As most viral particles are composed of a multitude of targeting elements, equipping NPs with more than one targeting ligand as well could therefore be a viable option. However, most viral cell recognition strategies show a considerable level of complexity with a highly orchestrated sequence of consecutive binding events to a multitude of cell surface structures.[9−12] Taking this into consideration, virus-mimetic nanomaterials should ideally also comprise targeting

elements, whose course of interaction with their target structures is adequately controllable.[13,14] While many approaches using multi-ligand NP systems already exist,[15−17] our focus lies not only on the manufacture of NPs with two different ligands but also on the precise steerability of ligand−receptor interactions, which, in our view, is crucial for the described viral target specificity.

In this context, we recently presented influenza A-mimetic NPs, which were enzymatically activated by a target cell ectoenzyme, thereby unveiling an additional ligand that triggered particle endocytosis via contact with its cell membrane receptor. This conditional and sequential target-cell recognition process led to a highly specific cell uptake *in*

vitro, even in the presence of a 10-fold surplus of off-target cells.[18] In a follow-up study, we refined these enzymatically activated NPs to reach mesangial cells *in vivo*.[19]

The mesangium was selected as the target with respect to its prominent role within the glomerulus as well as in the development of diabetic nephropathy and other related kidney diseases.[20−23] In this context, NPs accumulating in mesangial cells could possibly offer a starting point for a more rational therapy compared to the currently predominant gold standard, which is mainly based on control of blood pressure and glucose levels.[24] Even though the influenza A-mimetic concept resulted in an excellent NP accumulation in the mesangium, its underlying principle mandatorily requires the presence of an ectoenzyme on the cell of interest and thus is not broadly applicable to cells and tissues lacking respective enzymes.

Trying to overcome this major constraint, we were looking for a more versatile mechanism of endowing hetero-multi-valent NPs with the ability to sequentially bind a multitude of distinct cell surface structures. In that context, we decided to mimic human adenovirus type 2 (AdV2) as a biological model. To infiltrate possible target cells, AdV2 initially binds to the coxsackievirus and adenovirus receptor (CAR) via its terminal fiber knobs.[25−27] The laterally flexible virus−receptor complex then performs drifting motions alongside the cell membrane until it binds immobile integrins via its penton base RGD motif that finally triggers clathrin-mediated endocytosis.[28] We were particularly interested in the adenoviral infiltration strategy because the initial virus−cell interactions do not involve any processing or enzymatic conversion of the virus, as would be the case for the above-described influenza viruses or also SARS-CoV-2.[29] Additionally, the primary CAR binding does not initiate any endocytotic mechanisms but merely facilitates attachment to the cellular surface. To our estimation, this sequential process of primary attachment and subsequent uptake is highly promising to further increase the target specificity of nanomaterials. Trying to integrate this stepwise process into a robust NP system, the starting point of our considerations was that the visibility of ligands tethered to a NP surface can be readily controlled by altering the ligand density, the linker length, and the physical composition of the NP surface.[19,30] We therefore hypothesized that the intended stepwise particle−cell interaction could be achieved by sterically controlling the ligand−receptor binding events. To facilitate initial attachment to the cellular surface, we decided to use EXP3174, a losartan metabolite and potent blocker of the angiotensin II receptor type 1 (AT1r), which is known to be significantly upregulated in mesangial cells during various kidney pathologies such as diabetic nephropathy.[22,31] Due to its antagonistic features, EXP3174 should merely facilitate initial NP binding to AT1r, yet without immediate induction of uptake.[32] Based on the above-described adenoviral cell infiltration, cRGDfK (cyclo Arg-Gly-Asp-D-Phe-Lys), a well-established $\alpha_V\beta_3$ integrin agonist, was chosen to initiate integrin-mediated particle uptake of previously bound NPs.[33−35]

To enable primary AT1r binding, EXP3174 was tethered to longer block-copolymer chains, leading to the desired flexibility and consequently high availability of the AT1r antagonist. cRGDfK, in contrast, was bound to shorter block-copolymer strands and therefore was only able to reach $\alpha_V\beta_3$ integrins after a mandatory first AT1r binding and subsequent spatial approach of the NP to the cell membrane (Figure 1). This shielding of the second ligand should not only lead to the
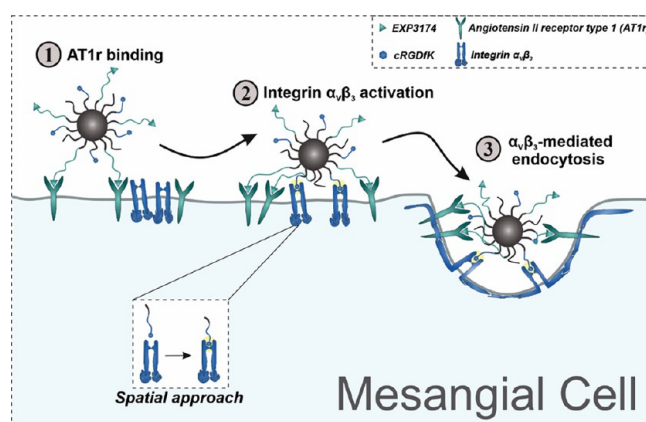

Figure 1. Adenovirus-mimetic NPs enter glomerular mesangial cells via a sterically controlled and thus sequential particle−cell interaction. NPs therefore initially bind the AT1r via EXP3174. After a subsequent spatial approach of the NP, $\alpha_V\beta_3$ integrin-mediated endocytosis is finally triggered via previously concealed cRGDfK.

described sequential particle−cell interaction but also prevent premature exposition to integrin-positive off-target sites such as angiogenic endothelial cells or macrophages.[36]

To investigate the feasibility of this recognition strategy, we used the same poly(ethylene glycol)−poly(lactic acid) (PEG-PLA) block-copolymer NP design and same target tissue as for our influenza A-mimetic concept. By doing so, we excluded any impact of unspecific factors such as differences in geometry or surface composition on the results.[37−39]

In the present study, we first evaluated the validity of our targeting strategy *in vitro* using mesangial cell mono-cultures as well as co-cultures that additionally comprised a major fraction of off-target cells. In a follow-up *in vivo* experiment, adenovirus-mimetic NPs were then tested for efficient accumulation in mesangial areas within the glomerulus (Figure S1), which should act not only as an adequate benchmark to compare our previous and new targeting concept but also as a prerequisite for future NP-based treatment of mesangial cells.

2. RESULTS AND DISCUSSION

2.1. Preparation of Hetero-multivalent EXPcRGD NPs Using a Modular Concept. To create NPs with the desired adenovirus-mimetic properties, we implemented a modular design that is based on the synergistic combination of different biocompatible polymer components into a hetero-multivalent particle species (Figure 2a). As a first component, biodegrad-able poly(lactic-*co*-glycolic acid) (PLGA) forms a hydrophobic NP core that not only guarantees enhanced structural integrity in aqueous media but also allows NP visualization via coupling of fluorescent dyes or nanogold.[40,41] PEG-PLA block copolymers as a second component offer the structural flexibility that is needed to implement our pursued virus-mimetic NP design.[42] In a first step, PEG-PLA polymers with either longer (PEG_{5k}-PLA_{10k}) or shorter (PEG_{2k}-PLA_{10k}) PEG chains were synthesized via ring-opening polymerization of cyclic lactide (Figure S2a and Figures S3−S6).[43]

Since EXP3174 was intended to initially bind the mesangial AT1r as a freely moving ligand, it was covalently coupled to the longer and thus more flexible PEG_{5k}-PLA_{10k} chains (Figure S2b). The second ligand (cRGDfK), in contrast, should not be able to interact with surface-bound integrins unless a first AT1r binding and subsequent spatial approach of the NP has taken
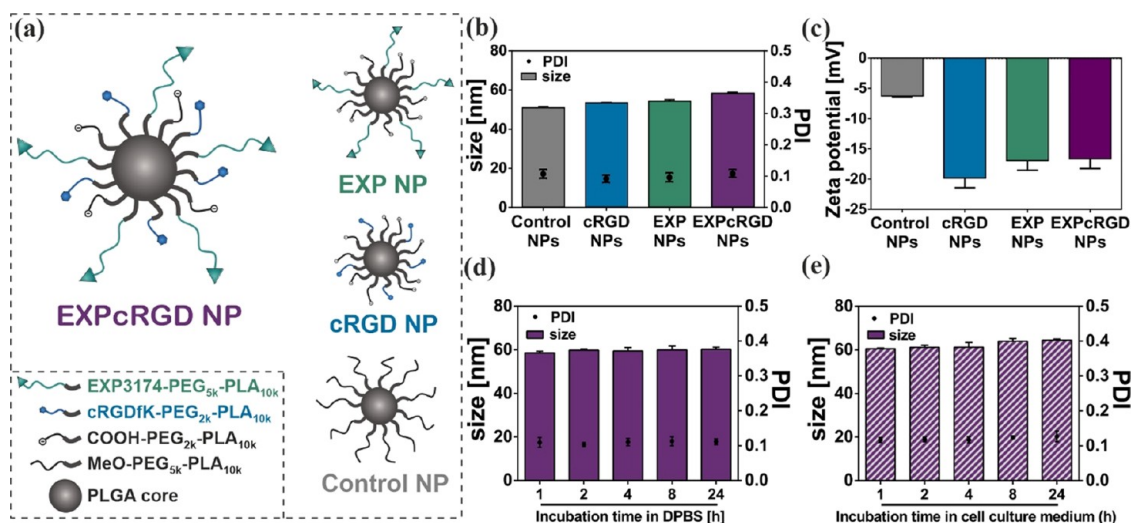
Figure 2. Characterization of different NP species. (a) Particle design of hetero-functional EXPcRGD NPs as well as homo-functional (EXP NPs and cRGD NPs) or nonfunctionalized NP species (Control NPs). (b) Dynamic light scattering (DLS) analysis. All particle types were manufactured below a size threshold of 60 nm without considerable aggregation (PDI, polydispersity index). (c) Zeta potential measurements. (d, e) NP stability analyzed through DLS measurements. EXPcRGD NPs underwent no significant size variation or aggregation upon incubation for 24 h at 37 °C in either (d) DPBS or (e) cell culture medium supplemented with 10% fetal bovine serum. Results represent mean ± SD (n = 3).

place. To that regard, it was attached to shorter PEG_{2k}-PLA_{10k} (Figure S2c). The NP surface density of both cRGDfK and EXP3174 could be tuned precisely by mixing distinct amounts of either ligand-functionalized or nonfunctionalized PEG-PLA polymers with PLGA prior to NP manufacture via nano-precipitation (Figure S2f–h).

Hetero-functional EXPcRGD NPs as well as homo-functional (EXP NPs/cRGD NPs) and nonfunctionalized, methoxy-terminated particles (Control NPs) were manufactured below a size threshold of 60 nm (Figure 2b). To our estimation, this size range was optimal for efficient extravasation from intraglomerular capillaries to reach mesangial areas as endothelial fenestrations have an average diameter of 60–100 nm.[44,45] Stability analysis in DPBS and cell culture medium (Figure 2d,e) as well as transmission electron microscopy (TEM) (Figure S2i) showed uniformly shaped NPs with no considerable tendency toward aggregation. Addition of unfunctionalized $COOH$-PEG_{2k}-PLA_{10k} to the polymer mix resulted in negative zeta potential values (Figure 2c). These characteristics should help further stabilize NPs and reduce unspecific binding to off-target cells. Also, extended serum protein adsorption and subsequent phagocytic clearance should be prevented.[37,46]

2.2. Hetero-multivalent EXPcRGD NPs Display Excellent Ligand Affinity for Target Motifs. While it has been previously demonstrated that homo-functional EXP3174- or cRGDfK-carrying NPs can be used to effectively target cell types expressing either AT1r or $\alpha_V\beta_3$,[47,48] we intended to prove that the merger of both ligands actually results in a hetero-multivalent nanomaterial that synergistically combines both ligands' features. We therefore initially evaluated the optimal surface density for each ligand to guarantee sufficient AT1r/integrin interaction. In the first step, we prepared homo-functional NPs with different ligand densities and performed DLS analysis to exclude any impact of the size differences on the later NP–cell interaction. As shown in Figure S7a,b, particle size and quality were not significantly altered by the respective ligand density for both cRGD NPs and EXP NPs. We then assessed EXP3174-mediated NP binding to the AT1r

expressed by rat mesangial cells (rMCs). As activation of G_q-coupled AT1r with its primary ligand angiotensin II (AT II) results in a calcium influx into the cell cytosol, intracellular Ca^{2+} levels after AT II stimulation can be used as a marker for AT1r activity after NP incubation. In that context, low receptor activity indicates a high ratio of bound EXP3174 as the ligand itself acts as a potent antagonist.[31]

Figure 3a shows intracellular Ca^{2+} levels of AT II-stimulated rMCs that had been pre-incubated with EXP3174-functionalized NPs or free EXP3174 for 45 min. Particles carried 25% of EXP3174 on their surface as this functionalization degree had been shown to sufficiently guarantee AT1r binding (Figure S7c). Both EXPcRGD NPs (IC_{50} = 276 ± 31 pM) and EXP NPs (IC_{50} = 552 ± 73 pM) showed excellent AT1r avidity, resulting in a highly effective inhibition of the receptor in the picomolar range and consequently minimal intracytosolic Ca^{2+} levels. Furthermore, inhibition potency of EXP3174-carrying NP types was even higher than for the free ligand (IC_{50} = 2.7 ± 0.9 nM). This strongly suggests that EXP3174-functionalized particles were able to interact with the target receptor in a multivalent fashion, leading to an overall avidity gain, which was in line with our previous findings.[49] As IC_{50} levels of both EXPcRGD and EXP NPs were found to be in the same range, we concluded that the combination of both EXP3174 and cRGDfK in one particle type did not significantly interfere with the binding capacity of EXP3174 itself. Interestingly, AT1r inhibition potency was even slightly higher for EXPcRGD NPs than for homo-functional EXP NPs. To our estimation, this effect was caused by the complete and irreversible removal of AT1 receptors from the cell surface due to the cRGDfK-mediated endocytosis of AT1r-bound NPs (Figure 1). Consequently, endocytosed receptors could no longer be (re)activated, leading to a sharper decrease in Ca^{2+} influx upon AT II stimulation. Control NPs and cRGD NPs did not show any interaction with the AT1r, resulting in a maximal Ca^{2+} signal upon receptor stimulation and confirming the assay's specificity for the AT1r (Figure S7d). Additionally, intracellular Ca^{2+} levels of AT1r-deficient HeLa cells were minimal upon EXPcRGD NP incubation and AT II stimulation, thereby
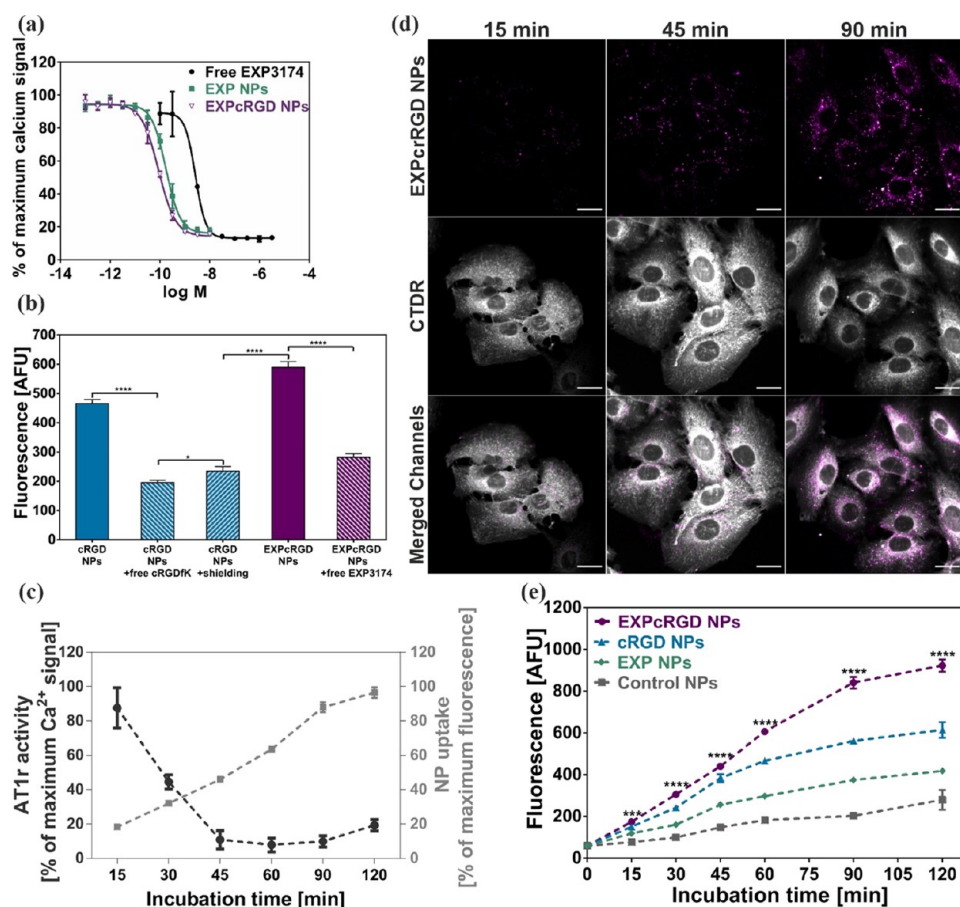
Figure 3. NP interaction with target motifs. (a) Intracellular calcium levels after AT1r stimulation of rMCs treated with free or particle-bound EXP3174. Both EXPcRGD NPs (IC_{50} = 276 ± 31 pM) and EXP NPs (IC_{50} = 552 ± 73 pM) effectively bound and therefore inhibited the AT1r. This effect was even stronger than for free EXP3174 (IC_{50} = 2.7 ± 0.9 nM) (M = molar concentration of either NPs or free EXP3174). (b) Flow cytometry analysis of rMC uptake for cRGD-carrying NPs. (c) Sequential NP−cell interplay. EXPcRGD NPs initially bound to the AT1r, leading to a drastic decline in AT1r activity via EXP3174 receptor blockade. In contrast, $\alpha_V\beta_3$-initiated NP uptake increased mainly after 45 min. (d) CLSM analysis of CTDR-stained rMCs after incubation with EXPcRGD NPs. Over time, increasing levels of NP-associated fluorescence (purple) could be detected in vesicular structures within the rMC cytosol (gray) (scale bar, 20 μm). (e) Flow cytometry analysis of NP uptake into rMCs over 120 min. Hetero-multivalent EXPcRGD NPs showed a substantially increased cell uptake compared to Control NPs as well as homo-functional NPs. Results represent mean ± SD (n = 3). *P < 0.05, ***P < 0.001, ****P < 0.0001 (AFU, arbitrary fluorescence units).

further supporting the AT1r binding specificity of EXPcRGD NPs (Figure S7e).

Having verified the AT1r binding capacity of adenovirus-mimetic EXPcRGD NPs, our next goal was to investigate particle uptake into rMCs via cRGDfK−$\alpha_V\beta_3$ interaction. As for EXP3174, we therefore initially evaluated the optimal cRGDfK ligand density for sufficient integrin-mediated NP endocytosis. As depicted in Figure S7f, cRGDfK-mediated rMC uptake of cRGD NPs gradually increased with higher ligand surface densities. In the next step, we introduced 25% of longer COOH-PEG$_{5k}$-PLA$_{10k}$ into these cRGDfK-functionalized NPs. This component should enable the above-described concept of steric hindrance and result in a reduced visibility of the cRGDfK ligand (Figure S8), which was central for our approach of a sequential ligand−receptor interplay. As shown in Figure S7g, ligand-mediated endocytosis could significantly be reduced for all cRGDfK densities, which we had tested before (Figure S7f). For the further course of our studies, we chose to prepare both cRGD NPs and EXPcRGD NPs with a cRGDfK density of merely 15% as this amount guaranteed a significantly enhanced ligand-mediated rMC uptake but could also be sufficiently regulated by addition of

respective shielding elements. As shown in Figure 3b, we finally compared levels of rMC uptake for the established NP compositions. As discussed above, cell uptake of cRGDfK-functionalized NPs could be significantly reduced by addition of described shielding elements. Interestingly, addition of an excess of free cRGDfK (c = 500 μM) prior to NP incubation led to a comparable decrease in cell uptake of unshielded cRGD NPs, thereby both proving the $\alpha_V\beta_3$-dependency of NP uptake and supporting the hypothesis that our shielding concept can equally inhibit ligand−integrin interaction. Remarkably, addition of EXP-PEG$_{5k}$-PLA$_{10k}$ instead of unfunctionalized COOH-PEG$_{5k}$-PLA$_{10k}$ (EXPcRGD NPs) reversed the shielding effect and significantly increased rMC uptake. We therefore concluded that hetero-functional EXPcRGD NPs initially bound the AT1r and subsequently were able to spatially approach the cell surface, thereby reaching the endocytosis-mediating integrin. This assessment was further supported by the observation that addition of free EXP3174 (c = 1 mM) prior to NP incubation led to a sharp decrease in EXPcRGD NP cell uptake as NPs were no longer able to bind the AT1r and approach the rMC surface. To additionally confirm our concept of a sequential ligand−
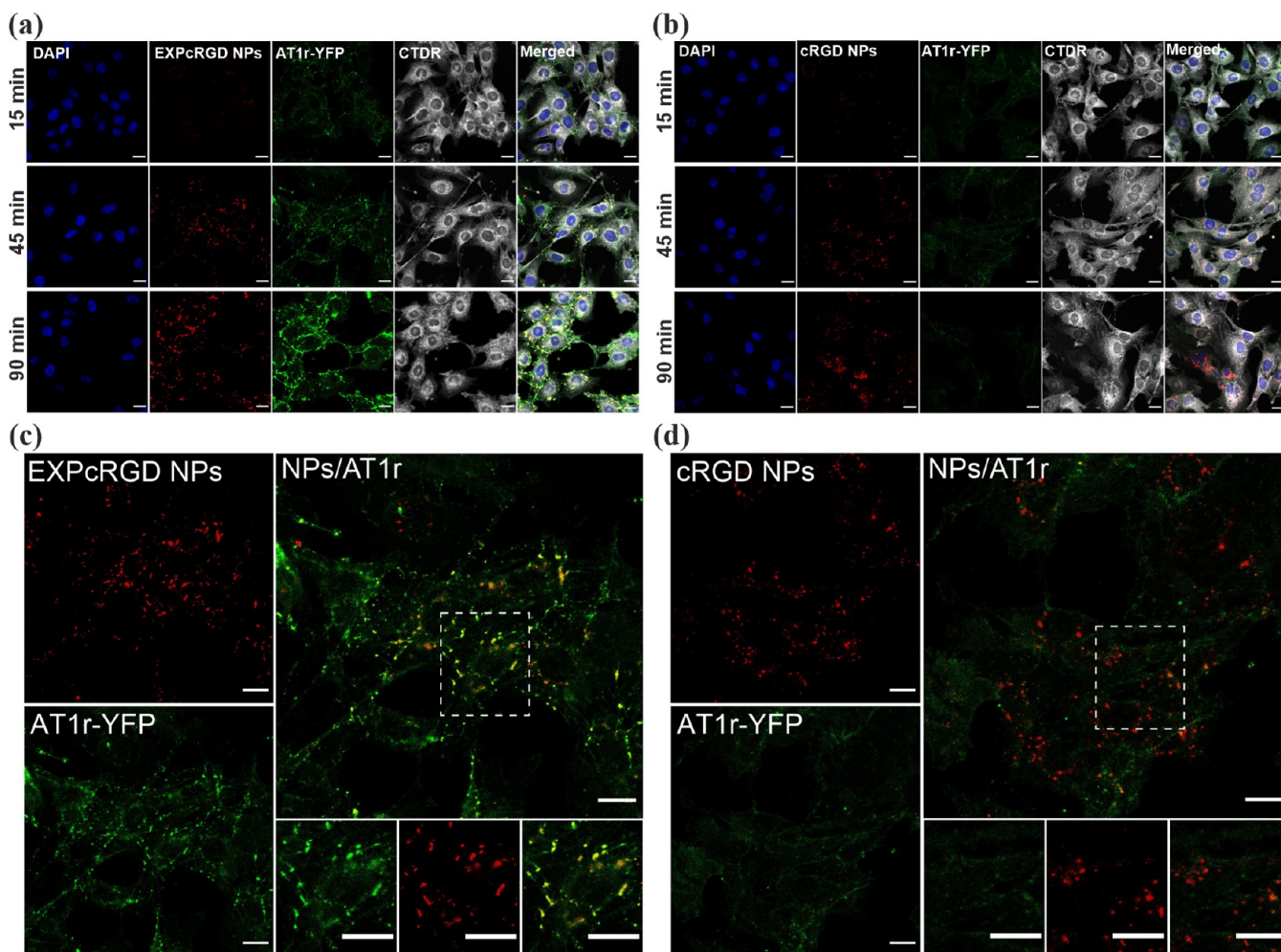
Figure 4. CLSM analysis of NP uptake (red) in rMCs (gray) transfected with YFP-tagged AT1r (green). (a) Time-dependent uptake of EXPcRGD NPs. Signals for both EXPcRGD NPs and AT1r-YFP significantly increased with longer incubation times. Fluorescence therefore intensified in mainly spherical structures, indicating AT1r clustering and subsequent NP/AT1r endocytosis. (b) Time-dependent uptake of cRGD NPs. While cRGD NP-associated fluorescence increased similarly to (a), no considerable change in AT1r-YFP signal could be detected. (c) EXPcRGD NP/AT1r localization after 45 min. Fluorescence signals for EXPcRGD NPs and the AT1r were exactly colocalized (yellow merged regions), proving NP-AT1r binding and subsequent endocytosis. (d) cRGD NP/AT1r localization after 45 min. cRGD NP-associated fluorescence showed no considerable colocalization with the AT1r signal, indicating an AT1r-independent uptake of NPs (scale bar, 20 μm). (Smaller images show a zoomed-in view of the white boxes above.)

receptor interplay, we compared the decrease in AT1r activity of rMCs due to EXP3174-mediated NP binding with the cRGDfK-mediated cell uptake of hetero-functional EXPcRGD NPs. As shown in Figure 3c, AT1r activity sharply decreased within the first 45 min and subsequently stayed on a minimal level. NP uptake, on the contrary, gradually increased with cell-associated fluorescence levels increasing even further after 45 min. This contrary time course further proved our assumption that hetero-functional NPs initially bound the AT1r and only then initiated cell uptake via integrin activation. Interestingly, AT1r activity slightly increased again at 120 min, which we explained with a possible AT1r recycling after completed uptake with bound NPs.

For better visualization of the time-dependent NP uptake, mesangial cells were incubated with fluorescently labeled NPs and the cellular distribution was analyzed via confocal laser scanning microscopy (CLSM). To exactly assess the dimensions of the cell body, rMCs were pretreated with CellTracker Deep Red (CTDR). Figure 3d shows strong intracellular accumulation of AlexaFluor 568-labeled

EXPcRGD NPs in spherical structures, which represent endocytotic vesicles.[50] Over time, both the number and intensity of visible accumulations increased. Especially between 45 and 90 min of incubation, vesicles appeared to considerably gain size. These findings demonstrate that after successful AT1r binding, EXPcRGD NPs could efficiently bind to the integrin receptor, triggering internalization through integrin-mediated endocytosis and accumulation in intracellular vesicles. It is well described in the literature that these endocytic vesicles can fuse to larger endosomes and therefore gain size as well as intensity over time.[51,52] Finally, we performed flow cytometry analysis of NP-treated rMCs and determined the cell-associated fluorescence over an incubation period of 120 min. As shown in Figure 3e, levels of NP-derived fluorescence were the highest for EXPcRGD NPs compared to all other NP species over the entire incubation period. While EXP NPs as well as Control NPs merely showed moderate fluorescence signals, substantial levels of cell association could be detected for cRGD NPs. However, respective fluorescence levels reached a plateau after approximately 60 min, while

EXPcRGD NPs' cell association further increased. This strongly supports our hypothesis of a sequential interaction between EXPcRGD NPs and their target cell, which results in a prolonged increase in fluorescence levels compared to homo-functional cRGD NPs.

2.3. Ultrastructural Analysis Indicates a Sequential Ligand−Receptor Interplay. To further verify the concept of sequential AT1r binding and integrin-mediated NP endocytosis, we performed time-dependent CLSM analysis of NP interaction with rMCs expressing the AT1r tagged with yellow fluorescence protein (AT1r-YFP rMCs). Figure 4a shows a significant accumulation of EXPcRGD NPs in intracellular vesicles over time, which was similar to the results depicted in Figure 3d. Additionally, AT1r-derived fluorescence considerably increased and intensified in also mainly spherical structures. While cRGD NPs showed a comparable intra-cellular accumulation with increasing incubation times (Figure 4b), no considerably enhanced AT1r signal could be detected. For better visualization of observed differences, we assessed the exact localization of both NP-associated and AT1r fluorescence after 45 min of incubation. As depicted in Figure 4c, signals for EXPcRGD NPs and the AT1r were exactly colocalized, indicating that these hetero-functional NPs had initially bound the AT1r and only then initiated integrin-mediated endocytosis, leading to an uptake of both EXPcRGD NPs and bound AT1r into spherical endocytotic vesicles (Figure 1). Homo-functional cRGD NPs, on the contrary, merely bound the integrin and initiated cell uptake, however without any interaction with the AT1r, whose fluorescence signal accordingly was not colocalized to a significant extent (Figure 4d). As a control, we additionally analyzed NP−cell interaction for cRGDfK-lacking EXP NPs and Control NPs (Figure S9).

While Control NPs did not show any significant rMC uptake or changes in AT1r signal over time (Figure S9b), considerable EXP NP-derived fluorescence was visible, however mainly located on the cell surface. This NP-associated fluorescence was colocalized with AT1r clusters, which had formed as a consequence of noninternalized, AT1r-bound NPs lacking additional cRGDfK functionalization (Figure S9a).

Finally, TEM analysis was performed to assess NP−cell interactions at an ultrastructural level.[53−55] Therefore, we used a NP labeling concept that we had recently established. To increase the electron density and consequential TEM visibility of applied NPs, ultrasmall gold NPs with an average diameter of 2.2 nm were covalently coupled to PLGA, which was then used for further NP manufacture (Figure S10a). Mesangial cells, which were incubated with these gold-tagged NPs, could then be gold-enhanced to intensify and thus visualize the particles' gold core and assess their exact location. This retrospective gold enhancement offers the substantial advant-age that physicochemical characteristics of nanogold-labeled NPs do not significantly differ from unlabeled NPs (Figure S10b), which would not be the case for commonly used larger gold NPs.

Figure 5a shows the cell body of two mesangial cells incubated with gold-tagged EXPcRGD NPs. Within the cell cytosol, numerous circular vesicles, filled with gold-enhanced NPs, could be detected. The distribution pattern showed remarkable similarity to the previously described CLSM results (Figures 3c and 4), thereby strongly supporting our hypothesis of ligand-mediated NP endocytosis. Additionally, a major fraction of particles was present at the cell border, indicating that these NPs were still bound to membrane-located surface
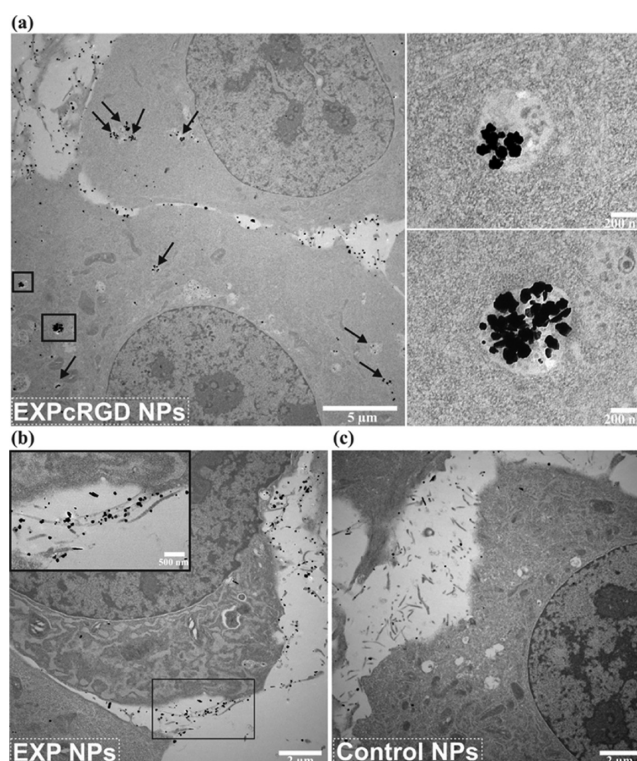

Figure 5. TEM analysis of NP interaction with mesangial cells. (a) EXPcRGD NPs accumulated in numerous vesicular structures (black arrows) within rMCs. Vesicles of differing sizes were present both in outer and inner parts of the cell cytosol, indicating intracellular processing and fusing into larger endosomes. Moreover, a substantial number of NPs were still located at the cell membrane, suggesting that particle underwent a stepwise process of initial cell binding and subsequent endocytosis. (Images on the right show a zoomed-in view of black boxes on the left.) (b) EXP NPs, in contrast, merely accumulated at the cell border where they bound to distinct surface structures of rMCs, indicating a possible interaction with membrane-bound AT1r. (Image in the top left corner shows the zoomed-in view of black box.) (c) Control NPs showed only negligible interaction with rMCs with hardly any gold-enhanced NPs visible.

structures that most likely represent AT1r clusters. These findings further indicate that EXPcRGD NPs interacted with the target cell in a stepwise process of prior binding to the AT1r and subsequent integrin-mediated endocytosis.

In accordance with this assessment, EXP NPs lacking the cRGDfK ligand could only be detected at the rMC membrane, while no significant particle accumulations in endocytotic vesicles were found (Figure 5b). Additionally, cell−particle association for Control NPs was only marginal (Figure 5c), which was also in line with our previous findings. cRGD NPs, in contrast, did accumulate in the rMC cytosol similar to EXPcRGD NPs but showed only marginal binding to the cell surface as these particles lacked AT1r ligand EXP3174 (Figure S11a). Particle-free cells were treated and prepared equally to demonstrate that the gold enhancement did not lead to unspecific staining (Figure S11b).

2.4. Virus-Mimetic Targeting Concept Facilitates Enhanced Mesangial Cell Specificity *In Vitro*. Having demonstrated that hetero-multivalent EXPcRGD NPs synerg-istically combine both key features of their surface ligands and present them in a sterically controlled manner, we intended to demonstrate that this design can actually be applied to increase mesangial cell specificity. We therefore implemented an *in*
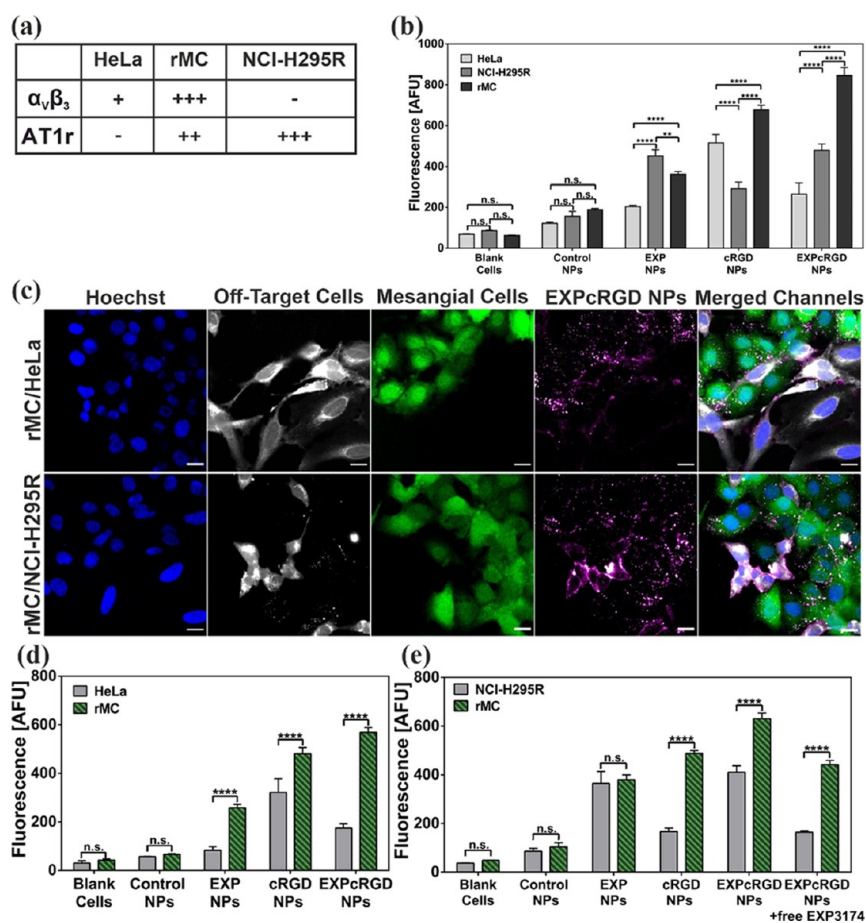
Figure 6. *In vitro* NP cell specificity in a mono- and co-culture assay. (a) Receptor expression of off-target HeLa and NCI-H295R cells in contrast to receptor double-positive rMCs. (b) Flow cytometry analysis of NP uptake in mono-culture. EXPcRGD NPs showed maximum uptake into target rMCs. (c) CLSM analysis of CTG-stained rMCs (green) co-cultured with CTDR-labeled HeLa or NCI-H295R cells (gray). Cell nuclei were stained with Hoechst 33258 (blue). For the rMC/HeLa co-culture (top row), NP-derived fluorescence (purple) could merely be detected within areas of rMCs. The co-culture of rMCs with AT1r-expressing NCI-H295R cells led to a diverging NP distribution (bottom row) with EXPcRGD NPs also binding to the surface of NCI-H295R cells, yet without any visible cell uptake (scale bars, 20 μm). Flow cytometry analysis of rMCs co-cultured with either (d) HeLa or (e) NCI-H295R cells supported CLSM results as EXPcRGD NPs showed a significantly higher cell association with rMCs in both cases. Results represent mean $\pm$ SD ($n = 3$). **$P < 0.01$, ****$P < 0.0001$ (n.s., not significant; AFU, arbitrary fluorescence units).

vitro-based assay, in which target rMCs were co-cultured with a superior number (5–10-fold) of off-target cells carrying merely one of the two target receptors. While HeLa cells express no AT1r and only low levels of $\alpha_V\beta_3$-integrin, NCI-H295R cells were chosen as they show high AT1r but no $\alpha_V\beta_3$ expression[18,47] (Figure 6a and Figure S12). To test the impact of different receptor expression levels on NP uptake, all cell lines were initially cultivated in mono-culture and incubated with different NP formulations (Figure 6b). Particle uptake in rMCs was in accordance with previous results, showing the highest levels of cellular internalization for EXPcRGD NPs. On the contrary, HeLa cells were only able to take up cRGD NPs efficiently. EXPcRGD NP uptake was thereby drastically reduced, which can be explained by a combined effect of the cRGDfK shielding and a missing AT1r expression. NCI-H295R cells, on the contrary, showed high levels of cell-associated fluorescence for EXP NPs and EXPcRGD NPs as these particle species could bind the abundantly present AT1r on the cell surface. In a next step, target rMCs were co-cultured with a superior number of either HeLa or NCI-H295R cells to test the NP's rMC specificity. To differentiate between co-cultured cells in CLSM analysis, CellTracker

Green (CTG) was used to stain rMCs, while off-target cells were marked with CTDR. After incubation with fluorescently labeled EXPcRGD NPs, cellular distribution of NPs was assessed. In the rMC/HeLa co-culture model, EXPcRGD NP-derived fluorescence could almost exclusively be detected within the areas of mesangial cells. HeLa cells, in contrast, showed merely weak interaction with NPs, resulting in marginal fluorescence levels (Figure 6c, top row). We accordingly concluded that EXPcRGD NPs could specifically locate mesangial cells among HeLa cells due to the differences in AT1r expression on the cell surface. These findings were supported by flow cytometry analysis, showing that cell-associated fluorescence of EXPcRGD NPs was significantly higher in rMCs than in off-target HeLa cells, while accumulation of cRGD NPs was considerable in both HeLa cells and rMCs (Figure 6d).

In contrast, rMC/NCI-H295R co-culture provided a divergent particle distribution. NP-associated fluorescence could not only be found in rMCs but also in areas covered by NCI-H295R cells. However, distribution patterns differed significantly. While fluorescence among rMCs was found in circular, vesicle-like structures as seen before, NCI-H295R-
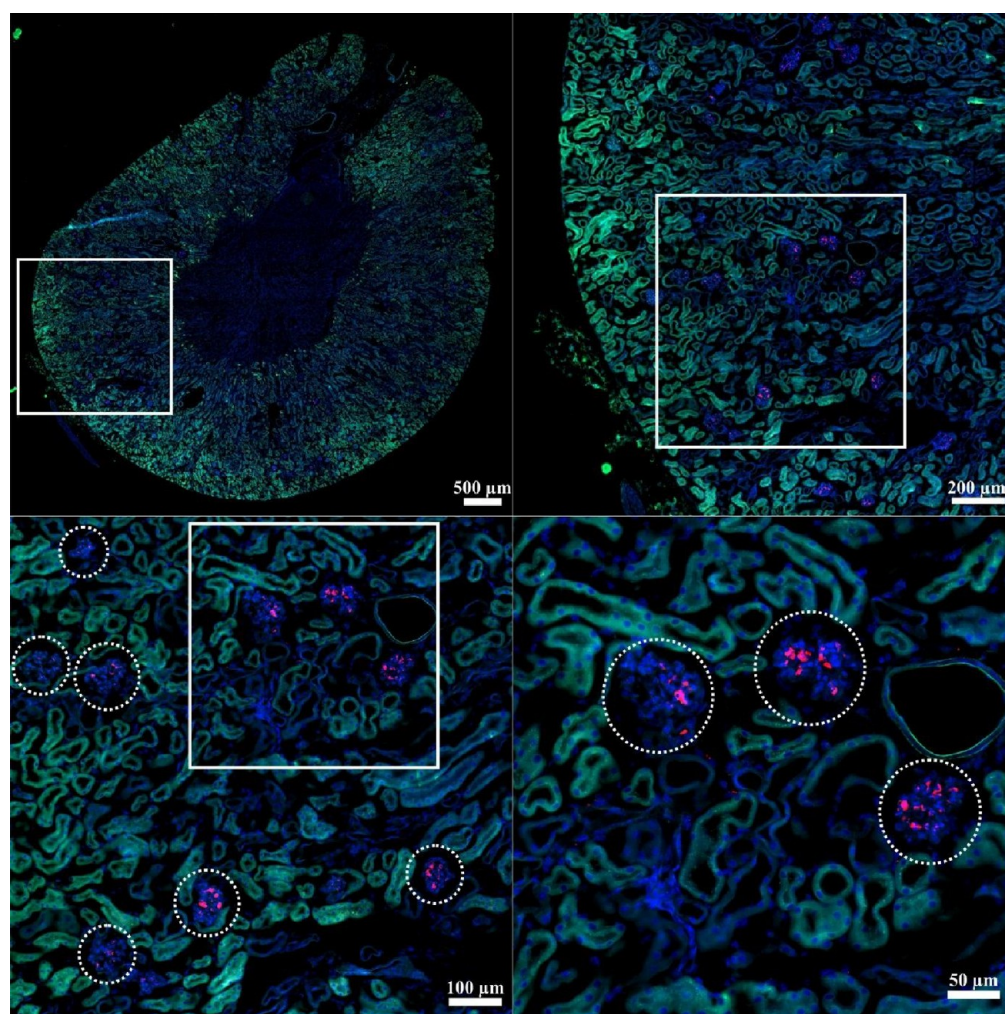
Figure 7. EXPcRGD NPs show strong intraglomerular accumulation *in vivo*. Transversal kidney cryosections were imaged using fluorescence microscopy. To facilitate histological evaluation, cell nuclei were stained with DAPI (blue) and tissue autofluorescence was recorded (green). EXPcRGD NPs (red) accumulated almost exclusively in glomerular areas of the cortex (white circles), while fluorescence in tubular areas was negligible. (From top left to bottom right, images show zoomed-in views of white boxes.)

associated fluorescence was more diffuse and intensified mainly at the cell membrane (Figure 6c, bottom row). We therefore concluded that while accumulating in endocytotic vesicles of rMCs as seen before, EXPcRGD NPs were merely able to bind AT1r present in the cell membrane of NCI-H295R cells but could not be taken up into the cytosol due to the absence of $\alpha_V \beta_3$ integrin. Additionally, flow cytometry analysis showed that even though EXPcRGD NP-associated fluorescence for NCI-H295R cells was higher compared to HeLa cells, EXPcRGD NPs still showed a significantly enhanced signal in mesangial cells (Figure 6e). EXP NPs, in contrast, bound to both rMCs and NCI-H295R cells with no significant cell specificity. Interestingly, addition of an excess of free EXP3174 ($c = 1$ mM) prior to EXPcRGD NP incubation led to a sharp decrease in fluorescence levels for NCI-H295R cells, while cell-associated fluorescence for rMCs was still significantly higher.

In summary, the co-culture model demonstrated that hetero-multivalent EXPcRGD NPs have the capability to effectively identify receptor-positive mesangial cells in the presence of off-target cells that are not only prevailing in number but even express one of the two target receptors. The sequential ligand–receptor interplay is therefore a decisive tool to minimize off-target accumulation as NPs are only taken up into cells that

express the necessary surface characteristics. If one receptor is missing, then NP uptake is drastically reduced, thereby maximizing cell specificity for receptor-positive target cells.

2.5. Accumulation of Adenovirus-Mimetic EXPcRGD NPs in Renal Mesangial Cells *In Vivo*. Both rMC binding and uptake studies successfully showed that the virus-mimetic concept of sequential ligand–receptor interaction enables hetero-multivalent EXPcRGD NPs to specifically target mesangial cells *in vitro*. However, transferring *in vitro* results into a robust system with sufficient *in vivo* efficiency has been shown to be the major obstacle in NP design as many strategies fail to deliver desired target specificity.[56] While many targeting studies oftentimes focus on the time-dependent biodistribution of targeted NPs upon administration, we were mainly interested in the question whether our adenovirus-mimetic NP species is able to specifically accumulate in mesangial cells *in vivo* or not. To our estimation, reaching mesangial areas within the glomerulus requires not only adequate passive accumulation in the target region but also described active cell uptake and is therefore an ideal benchmark to enable the comparison between our novel adenovirus NPs and the previously tested influenza A-mimetic design.

To that regard, NPs were initially tested for potential cytotoxicity to guarantee the pharmaceutical safety of the NP system. Both nonfunctionalized Control NPs and EXPcRGD NPs showed no significant reduction of cell viability (Figure S13). In the next step, fluorescently labeled NPs were injected into 10-week-old female NMRI mice. After 1 h of NP circulation, mice were sacrificed, and kidneys were extracted. Fluorescence analysis of prepared cryosections revealed that EXPcRGD NPs effectively accumulated in glomerular areas, while fluorescence in tubular parts of the kidney was negligible (Figure 7). On the contrary, Control NPs as well as homo-functional EXP or cRGD NPs showed a considerably lower deposition in kidney cryosections (Figure S14).

To quantify observed differences, we determined glomerulus-associated fluorescence levels by assessing the glomerular fluorescence intensity per area for all NP types (Figure 8a,b).
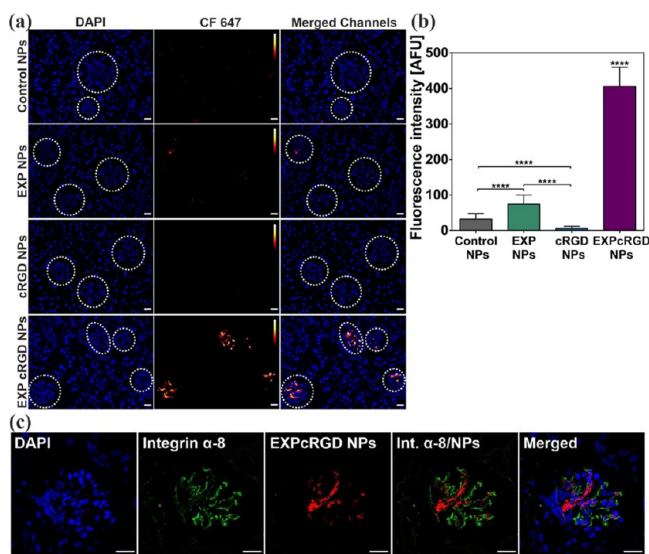

Figure 8. EXPcRGD NPs show a significantly enhanced accumulation in mesangial cells. (a) Fluorescence microscopy analysis revealed that high fluorescence levels within glomeruli (white circles) could mainly be detected for EXPcRGD NPs. While EXP NPs showed a moderate accumulation in glomeruli, Control NPs and cRGD NPs did not produce signals to any considerable extent (scale bar, 20 μm; calibration bar, 0−65,535 Gray value). (b) Precise quantification of intraglomerular fluorescence intensity was achieved by assessing the integrated density per area of glomerulus for 60 glomeruli per sample. Therefore, EXPcRGD NPs showed far higher fluorescence intensities per glomerulus compared to all other particle types. Results represent mean ± SD ($n = 60$). ****$P < 0.0001$ (AFU, arbitrary fluorescence units). (c) Antibody staining for mesangial surface marker integrin α-8 showed that EXPcRGD NP-associated fluorescence (red) was found within areas covered by mesangial cells (green), indicating that EXPcRGD NPs were able to specifically infiltrate mesangial cells via endocytosis. Scale bar, 20 μm.

EXPcRGD NPs thereby showed a more than 10-fold increase in fluorescence intensity compared to Control NPs. Moreover, glomerular accumulation of hetero-multivalent NPs was significantly greater than for both homo-functional NP types. Remarkably, cRGD NP fluorescence was even lower than for nonfunctionalized Control NPs. We therefore hypothesized that cRGD NPs were not able to reach glomerular areas as a predominant number of particles bound $\alpha_V\beta_3$-expressing cells such as angiogenic endothelial cells shortly after injection and consequently left the bloodstream before reaching deeper areas

of the kidney.[57] This hypothesis was further supported by the finding that relative blood plasma levels of cRGD NPs after 1 h of incubation were the lowest among all particle types (Figure S15). In EXPcRGD NPs, on the contrary, shorter cRGDfK-functionalized PEG-PLA chains were shielded from premature exposition to $\alpha_V\beta_3$ integrins by addition of longer, EXP3174-functionalized PEG-PLA chains. Consequently, hetero-multivalent particles avoided off-target deposition and therefore successfully reached glomerular areas within the kidney. Antibody staining for mesangial cell marker integrin-α8 further revealed that EXPcRGD NP-associated fluorescence in the glomerulus could almost entirely be found within mesangial cells (Figure 8c), proving our hypothesis of extravasation into the mesangial interstitium and subsequent endocytosis (Figure S1). To verify that detected fluorescence in mesangial areas was derived from structurally intact NPs, we additionally injected a comparable dose of free fluorescent dye into mice and analyzed fluorescence deposition. While the intra-glomerular signal for these samples was negligible, tubular cells exhibited very strong fluorescence levels (Figure S16). This indicated that, in contrast to injected NP species, the low-molecular dye was filtrated into the tubular system. We therefore concluded that intraglomerular fluorescence for all NP types derived from intact particles as degradation would have led to an increase in the tubular signal, otherwise.

To our estimation, discussed *in vivo* studies successfully demonstrated the potential of our new adenovirus-mimetic NP design. Hetero-multivalent EXPcRGD NPs effectively accumulated in mesangial areas of the glomerulus, while homo-functional or unfunctionalized NP species failed to do so. This strongly suggests that to reach sufficient levels of bioavailability, NPs do not only have to carry appropriate surface ligands but must also present them in an orchestrated fashion that is suitable for the respective targeting strategy. Moreover, NP accumulation in the mesangium also proved that our adenovirus-mimetic system of sterically controlled particle—cell interaction represents a viable alternative to our previously published influenza A-mimetic concept that was limited to a previous enzymatic activation.

3. CONCLUSIONS

In this study, we manufactured adenovirus-mimetic block-copolymer NPs capable of effectively targeting glomerular mesangial cells due to a sterically controlled, sequential ligand—receptor interaction, which is independent of previous enzymatic ligand activation. Hetero-multivalent NPs not only showed precisely tunable physicochemical characteristics but also displayed excellent avidity for both target motifs, leading to a substantial AT1r binding in the picomolar range and a significantly increased mesangial cell uptake compared to unfunctionalized NPs. Profiting from these features, virus-mimetic NPs could specifically target mesangial cells *in vitro*, even in a surrounding environment of off-target cells. Additionally, hetero-multivalent NPs displayed the necessary *in vivo* robustness, leading to an efficient accumulation in mesangial areas *in vivo* with only marginal off-target deposition within the kidney. Remarkably, hetero-multivalent EXPcRGD NPs showed far better mesangial targeting compared to homo-functional cRGD or EXP NPs, although these previously had been found to also display substantial activity for receptor-positive cell lines *in vitro*.[30,49] These findings strongly support our conviction that to exhaustively profit from their ligand features *in vivo*, nanomaterials have to utilize them in an

appropriate biomimetic manner. Our new concept of sterically controlled particle−cell interaction proved to be a viable alternative to our previous design of enzymatic ligand activation as it also led to a significant NP accumulation in the mesangium. As we were able to target the same distinct cell type *in vivo* with two divergent virus-inspired concepts, we conclude that mimicry of viral infection patterns can offer promising starting points for further targeting concepts and should therefore be more thoroughly investigated. Moreover, our successful mesangial cell targeting moves a more refined therapy of mesangium-related kidney pathologies within reach as it could dramatically increase drug delivery compared to all other currently available approaches. In that regard, we could already show that the antifibrotic and therefore highly promising drug candidate pirfenidone (PFD) can efficiently be encapsulated in presented block-copolymer NPs using both the above-described nanoprecipitation and a novel microfluidic technique.[58] Especially when it comes to highly active substances such as PFD, drug delivery approaches using described virus-mimetic NPs could significantly decrease unfavorable off-target accumulation, thereby drastically improving currently available therapy options.

4. EXPERIMENTAL SECTION

4.1. Materials. Heterobifunctional hydroxyl poly(ethylene glycol)-carboxylic acid with molecular mass of 2000 and 5000 g mol^{-1} (COOH-$PEG_{2k/5k}$-OH) and hydroxyl poly(ethylene glycol)Boc-amine with a molecular mass of 2000 g mol^{-1} (Boc-NH-PEG_{2k}-OH) were purchased from Jenkem Technology USA Inc. (Allen, TX, USA), while methoxy poly(ethylene glycol)with a molecular mass of 5000 g mol^{-1} (MeO-PEG_{5k}-OH) and Resomer RG 502 (PLGA; lactide:glycolide, 50:50; molecular mass, 13,400 g mol^{-1}) were obtained from Sigma-Aldrich (Taufkirchen, Germany). EXP3174 (also known as losartan carboxylic acid) was purchased from Santa Cruz (Heidelberg, Germany), while cyclic RGDfK (cRGDfK) was obtained from Synpeptide Co. Ltd. (Shanghai, China). AlexaFluor 568 Hydrazide (Alexa568), CellTracker Green Dye (CTG), and CellTracker Deep Red Dye (CTDR) were purchased from Fisher Scientific GmbH (Schwerte, Germany).

Amine-functionalized spherical gold NPs with an average diameter of 2.2 nm ($Au_{2.2}$-NH_2) were obtained from Nanopartz Inc. (Loveland, CO, USA). GoldEnhance EM Plus kit was purchased from Nanoprobes (Yaphank, NY, USA). Goat-derived integrin α-8 antibody was obtained from R&D Systems (Minneapolis, MN, USA). All other chemicals were purchased from Sigma-Aldrich in analytical grade if not stated differently. Ultrapure water was obtained from a Milli-Q water purification system (Millipore, Billerica, MA, USA).

Rat-derived mesangial cells (rMCs) were a kind gift from Prof. Dr. Armin Kurtz (Institute of Physiology, University of Regensburg, Regensburg, Germany). NCI-H295R (CRL-2128) and HeLa (CCL-2) cells were purchased from ATCC (Manassas, VA, USA). All cell lines were cultured in RPMI 1640 medium containing 10% fetal bovine serum, insulin-transferrin-selenium (ITS) (1×), and 100 nM hydrocortisone. AT1r-YFP rMCs were generated by transfecting rMCs with a plasmid encoding the AT1r with a YFP-tag (CXN2-HA-AT1R-YFP) using Lipofectamine 2000 according to the manufacturer's instructions and as previously described.[19] For culture of AT1r-YFP rMCs, RPMI1640 medium was additionally supplemented with Geneticin (600 μg mL^{-1}).

4.2. Polymer Synthesis. COOH-PEG_{2k}-PLA_{10k}, Boc-NH-PEG_{5k}-PLA_{10k}, and MeO-PEG_{5k}-PLA_{10k} block copolymers were synthesized via a ring-opening polymerization as previously described.[37,43] In brief, heterobifunctional PEG polymers (1 equiv) were mixed with 3,6-dimethyl-1,4-dioxane-2,5-dione (70 equiv) and 1,8-diazabicylo [5.4.0] undec-7-ene (3 equiv). The polymer mixture was stirred for 1 h at room temperature (RT) until polymerization was quenched with

benzoic acid (14 equiv). The resulting block copolymer was precipitated in diethyl ether, isolated via filtration, and dried under vacuum. The molecular weight of synthesized polymers was determined in deuterated chloroform at 295 K using a Bruker Avance 300 spectrometer (Bruker BioSpin GmbH, Rheinstetten, Germany).

For preparation of cRGDfK-PEG_{2k}-PLA polymers, previously synthesized COOH-PEG_{2k}-PLA_{10k} was covalently coupled to the lysine residue of cRGDfK, as shown before.[30,59] In short, COOH-PEG_{2k}-PLA_{10k} (1 equiv) was activated using 3-(ethyliminomethyle-neamino)-*N,N*-dimethylpropan-1-amine (EDC)/*N*-hydroxysuccini-mide (NHS) (25 equiv) for 2 h at RT, followed by quenching with β-mercaptoethanol (BME) (30 equiv). The activated polymer was reacted with cRGDfK (3 equiv) and *N,N*-diisopropylethylamine (DIPEA) (10 equiv) for 24 h at RT. After precipitation of the resulting cRGDfK-coupled polymer in diethyl ether/methanol (15:1, v/v), free cRGDfK and excess reactants were removed using dialysis against Millipore water (mpH_2O).

For EXP3174-PEG_{5k}-PLA_{10k}, the Boc-protecting group of Boc-NH-PEG_{5k}-PLA_{10k} was initially cleaved. In brief, the Boc-protected polymer was dissolved in dichloromethane (DCM)/trifluoroacetic acid (TFA) (1:1, v/v). After stirring for 30 min (min), excess TFA was neutralized using a saturated sodium hydrogen carbonate solution. The organic phase was washed with mpH_2O, followed by polymer isolation, as described above.

Resulting NH_2-PEG_{5k}-PLA_{10k} was coupled to EXP3174 via the carboxylic acid residue of the imidazole component. EXP3174 (3.5 equiv) was activated with *N,N′*-dicyclohexylcarbodiimide (DCC)/NHS (3.3 equiv) for 2 h at RT. After removal of resulting dicyclohexylurea via centrifugation, NH_2-PEG_{5k}-PLA_{10k} (1 equiv) and DIPEA (17.5 equiv) were added and reacted for 24 h at RT. Resulting EXP3174-PEG_{5k}-PLA_{10k} was precipitated in methanol/diethyl ether (1:5, v/v) and the product was dialyzed against ethanol/100 mM borate buffer (pH 8.5)/water (1/1/8, v/v) for 24 h followed by mpH_2O for 12 h to remove unreacted EXP3174 and excess reactants.

4.3. PLGA Labeling with Fluorescent Dyes. For particle visualization, the core-forming PLGA was covalently linked to fluorescent dyes prior to NP preparation. To that end, carboxylic acid-terminated PLGA was activated for 2 h using 4-(4,6-dimethoxy-1,3,5-triazin-2-yl)-4-methylmorpholinium chloride (DMTMM) as a catalytical agent. Activated PLGA was then reacted with either AlexaFluor 568 Hydrazide or CF 647 amine for 24 h at RT. Labeled PLGA was dialyzed against mpH_2O for 24 h to remove unreacted fluorescent dyes.

4.4. PLGA Labeling with Nanogold. For electron microscopy analysis, PLGA was conjugated to nanogold according to a method that was previously established by our group.[41] PLGA was initially activated with EDC and NHS for 2 h in DCM. After DCM removal under reduced pressure, activated PLGA was dissolved in DMSO and mixed with DIPEA and lyophilized monoamino gold NPs with an average diameter of 2.2 nm ($Au_{2.2}$-NH_2). After stirring at RT for 24 h, gold-conjugated PLGA was precipitated in mpH_2O, isolated via centrifugation at 2500*g* for 10 min, and lyophilized.

4.5. NP Preparation. Block-copolymer NPs were manufactured using a common solvent evaporation technique. Corresponding amounts of PEG-PLA polymers and PLGA were mixed at a ratio of 70/30 (m/m) and diluted in acetonitrile (ACN) to a final concentration of 10 mg mL^{-1}. To reach the desired ligand surface density for hetero-/homo-functional NP species, cRGDfK-PEG_{2k}-PLA and/or EXP3174-PEG_{5k}-PLA_{10k} were mixed with COOH-PEG_{2k}-PLA_{10k} according to the calibration depicted in Figure 2d,e. The organic phase was then added dropwise by vigorous stirring to 10% Dulbecco's phosphate-buffered saline (DPBS) (v/v) (7.5 mM, pH 7.4) and stirred for 3 h at RT to remove the organic solvent.

Resulting NP dispersions were concentrated via centrifugation at 1250*g* for 25 min using Pall Microsep filters (molecular weight cut-off, 30 kDa; Pall Corporation, NY, USA). To obtain the mass concentration of manufactured NPs, a method previously introduced by our working group was used.[30] In brief, the PEG content was assessed using a colorimetric iodine complexing assay.[60] NPs were

then lyophilized and gravimetrically analyzed to obtain the ratio of PEG content and NP weight. In the following experiments, this ratio was used to calculate the mass concentration from the assessed PEG content for each NP species. The molar NP concentration was calculated as described before,[19] taking into account the NP mass concentration, an estimated NP density of 1.25 g cm^{-3}[61] as well as the NP diameter assessed by dynamic light scattering measurements, assuming a spherical NP shape.

4.6. NP Characterization. The NP size and zeta potential were evaluated using a Malvern Zetasizer Nano ZS (Malvern, Herrenberg, Germany). Samples were measured with a 633 nm He–Ne laser at an angle of 173° (25 °C, RT) in 7.5 mM DPBS using either PMAA semimicrocuvettes (DLS; Brand, Wertheim, Germany) or folded capillary cells (zeta potential; Malvern, Herrenberg, Germany), respectively. For stability analysis, NPs were prepared as described above and incubated for 24 h at 37 °C in DPBS as well as RPMI 1640 medium containing 10% fetal bovine serum. At the displayed time points, a sample was taken, and the size was evaluated as described above.

4.7. cRGDfK Quantification. The level of cRGDfK on the NP surface was assessed using a previously described method that is based on the measurement of arginine.[35] In brief, 50 μL of NP samples (1 mg mL^{-1}) was mixed with 175 μL of a working solution consisting of 9,10-phenanthrenequinone (150 μM in ethanol) and 2 N NaOH (6:1, v/v). After 3 h of incubation at 60 °C, 1 equiv of the sample was mixed with 1 equiv of 1 N HCl and incubated for another 1 h at RT. Finally, fluorescence was measured at a Synergy Neo2 Multi-Mode Microplate Reader (BioTek Instrument Inc., Winooski, VT, USA) with an excitation wavelength of 312/7 nm and an emission wavelength of 395/7 nm. Dilutions of cRGDfK (0–40 μg mL^{-1}) served as calibration. cRGDfK molarity and the ratios of molar cRGDfK content and molar PEG content were determined and plotted against the theoretical value (Figure S2h).

4.8. EXP3174 Quantification. To determine the surface level of EXP3174 on manufactured particles, 1 equiv of NP samples (1 mg mL^{-1}) was mixed with 10 equiv of 0.2 M acetic acid. Dilutions of EXP3174 in 0.2 M acetic acid (0–30 μM) served as calibration. Fluorescence of samples and standards was measured at a Synergy Neo2 Multi-Mode Microplate Reader (see above) (excitation, 250/10 nm; emission, 370/5 nm). EXP3174 molarity as well as the ratios of molar EXP3174 content and molar PEG content was determined and plotted against the theoretical value (Figure S2g).

4.9. Calcium Mobilization Assay. To investigate AT1r binding of NPs, intracellular calcium levels were measured using fura-2 as a Ca^{2+} chelator, as previously described by our working group.[49] In brief, rMCs were incubated with 5 μM fura-2 AM, 2.5 mM probenecid, and 0.05% Pluronics F-127 in Leibovitz's L-15 medium for 1 h at RT. Cells were thereafter centrifuged (5 min, 200g, RT) and resuspended in Leibovitz's medium. Forty-five microliters of NPs or free EXP3174 at different concentrations was pipetted into 96-well plates (Greiner Bio One, Frickenhausen, Germany), followed by 45 μL of rMC suspension (2×10^6 cells mL^{-1}). In the following, cells were incubated with samples for 45 min at RT. After incubation, 10 μL of 30 nM AT II was added to each well to activate uninhibited AT1r and consequently induce Ca^{2+} influx into the cell cytosol. The fluorescence signal during the first 30 s after injection was measured using a FluoStar Omega fluorescence microplate reader (BMG Labtech, Ortenberg, Germany) with excitation filters at 340/20 nm and 380/20 nm and the emission filter at 510/20 nm, respectively. The maximal ratio of Ca^{2+}-bound to Ca^{2+}-unbound Fura-2 was evaluated by incubating loaded cells with 0.1% Triton-X 100 and measuring fluorescence levels as described above. Analogously, the minimal ratio was achieved by incubation with 0.1% Triton-X 100 combined with 45 mM ethylene glycol-bis(2-aminoethylether)-N,N,N',N'-tetraacetic acid (EGTA). Levels of intracellular calcium per sample were calculated using the equation of Grynkiewicz et al.[62] Half-maximal inhibitory concentrations (IC$_{50}$) were calculated using GraphPad Prism (San Diego, CA, USA) and by applying a sigmoidal dose–response equation (variable slope).

4.10. CLSM Analysis. For a detailed analysis of NP–cell interaction, either rMCs or AT1r-YFP rMCs were seeded into eight-well slides (Ibidi, Gräfelfing, Germany) at a density of 15,000 cells well^{-1} and incubated for 24 h at 37 °C. To facilitate visualization of the cell cytosol, cells were stained with CTDR (25 μM, 45 min, 37 °C) in serum-free RPMI 1640 medium prior to seeding. NPs were manufactured using AlexaFluor 568-labeled PLGA and adjusted to 0.05 mg mL^{-1} in Leibovitz's buffer supplemented with 0.1% bovine serum albumin (BSA). Mesangial cells were incubated with 250 μL of NPs for 15, 45, and 90 min at 37 °C, washed with prewarmed DPBS, and fixed with 4% paraformaldehyde (PFA) in DPBS for 10 min. AT1r-YFP rMCs were additionally stained for cell nuclei with a 1:200 dilution of 4′,6-diamidine-2′-phenylindole dihydrochloride (DAPI) in DPBS. After the final washing step, fixed samples were analyzed using a Zeiss LSM 710 (Carl Zeiss Microscopy GmbH, Jena, Germany).

4.11. Flow Cytometry. To assess mesangial cell association of NP samples, rMCs were seeded into 24-well plates (Greiner Bio One, Frickenhausen, Germany) at a density of 40,000 cells well^{-1} and incubated for 48 h at 37 °C. NPs were manufactured using CF 647-labeled PLGA and adjusted to 0.05 mg NP mL^{-1} in Leibovitz's buffer supplemented with 0.1% BSA. To confirm $\alpha_V\beta_3$ dependence of NP cell entry, 300 μL of free cRGDfK (c = 500 μM) was added to the relevant cell samples for 15 min prior to NP incubation. Cells were washed with DPBS and 300 μL of prewarmed NP solutions was added for 45 min at 37 °C. For respective analysis of time-dependent uptake, cells were incubated over a time period of 120 min, with NPs being removed after 0, 15, 30, 45, 60, 90, and 120 min. Cells were washed with DPBS, trypsinized, and centrifuged for 5 min at 200g and 4 °C, followed by two further washing and centrifugation steps (DPBS, 200 g, 5 min, 4 °C). Final samples were resuspended in DPBS and analyzed using a FACS Calibur cytometer (Becton Dickinson, Franklin Lakes, NJ, USA). NP-associated fluorescence was excited at 633 nm and corresponding emission was recorded (661/16 bandpass filter). Flow cytometry data was analyzed using Flowing software 2.5.1 (Turku Centre for Biotechnology, Turku, Finland). Within the population of viable cells, the geometric mean of cell-associated fluorescence was evaluated.

4.12. Transmission Electron Microscopy. To evaluate cellular localization of NPs, rMCs were seeded into a 24-well plate at a density of 12,000 cells well^{-1} and incubated for 72 h. NP formulations containing nanogold-conjugated PLGA were diluted in Leibovitz's buffer containing 0.1% BSA and added for 45 min at a concentration of 0.05 mg mL^{-1} (V = 300 μL). After incubation, samples were washed with DPBS and prepared for electron microscopy analysis according to a pre-established protocol of our working group.[41] In brief, cells were fixed with 2.5% PFA and 2.5% glutaraldehyde in a 0.1 M sodium cacodylate solution (Caco buffer) for 60 min at RT, washed with Caco buffer, and permeabilized with 0.1% Triton-X in DPBS for 10 min. After a washing step with mpH$_2$O, samples were gold-enhanced using a GoldEnhance EM Plus kit (Nanoprobes Inc., Yaphank, NY, USA) according to the manufacturer's specifications, followed by further washing and post-fixation in a 2.5% sodium thiosulfate solution in mpH$_2$O. Cells were stained with 0.5% osmium tetroxide and dehydrated in rising concentrations of ethanol (50–99.5%). For counterstaining, 2% uranylacetate was applied for 5 min at 70% ethanol concentration. After embedding in Epon, ultrathin sections of 150 nm were imaged using a 100 kV Zeiss Libra 120 electron microscope (Carl Zeiss NTS GmbH, Oberkochen, Germany) at a magnification of 6300× as well as 12,500×. For exact analysis of the NP size without gold tag, EXPcRGD NPs were manufactured in mpH$_2$O as described above and adjusted to 50 μg mL^{-1}. Samples were thereafter pipetted onto carbon-coated copper grids (300 mesh; Plano, Wetzlar, Germany) and incubated for 2 min. Excess NPs were removed with a filter paper, and the grids were negatively stained with 1% uranyl acetate solution and stored in a desiccator until TEM analysis.

4.13. Co-culture Experiments. To assess cell specificity of manufactured NPs, we used a co-culture design that had been previously implemented by our group.[18] For mono-culture NP uptake (Figure 6b), pre-seeded rMCs, NCI-H295-R, or HeLa cells were

incubated for 45 min with different CF 647-labeled NP types. Cell uptake was then assessed using flow cytometry as described above.

For co-culture analysis, rMCs were seeded together with HeLa or NCI-H295R cells in 24-well plates at a density of 10,000 and 50,000/100,000 cells well^{-1}, respectively, and incubated for 48 h at 37 °C. To differentiate between cell types, rMCs were stained with CTG (15 μM, 45 min, 37 °C) in serum-free RPMI 1640 medium prior to seeding.

Co-cultured cells were then incubated with CF 647-labeled NPs at a concentration of 0.05 mg mL^{-1} (V = 300 μL) for 45 min. Preparation of samples and flow cytometry analysis were performed as described above. Additionally, rMC-associated fluorescence was excited at 488 nm and recorded using a 530/30 bandpass filter.

During data analysis, the population of viable cells was further gated for stained rMC cells and NP-associated fluorescence analyzed concerning cell specificity.

For CLSM analysis, rMC cells were CTG-stained prior to seeding as described above. To visualize all cell types, HeLa or NCI-H295R cells were also stained using CTDR (25 μM, 45 min, 37 °C). After CellTracker incubation, rMCs were seeded into eight-well Ibidi slides together with HeLa/NCI-H295R cells at densities of 2000 and 10,000/20,000 cells well^{-1}. After 48 h of incubation at 37 °C, cell nuclei were stained with Hoechst 33258 (5 μg mL^{-1} in DPBS) for 20 min. Cells were washed twice with prewarmed DPBS and AlexaFluor 568-labeled NPs were added at a concentration of 0.05 mg mL^{-1} (V = 250 μL) for 45 min at 37 °C. After NP incubation, samples were treated as described above and analyzed using a Zeiss LSM 710 microscope.

4.14. *In Vivo* Cell Targeting. Animal experiments were performed according to the national and institutional guidelines and approved by the local authority (Regierung von Unterfranken, reference number 55.2-2532-2-329). Ten week-old female NMRI mice (Charles River, Sulzfeld, Germany) acted as model animals. After analgesia with buprenorphine (0.1 mg kg body weight^{-1}), mice were anaesthetized with isoflurane and 100 μL of CF 647-labeled NPs (c = 120 nM) were injected via the vena jugularis (n = 6 for each NP species). Additionally, 100 μL of the free CF 647 dye was injected at a comparable concentration (50 μM). Mice were kept in anesthesia and after 5 min, an initial blood sample was taken via i.v. puncture. After 60 min, mice were anaesthetized with ketamine/xylazine, a final blood sample was taken, and animals were killed via perfusion fixation. Both kidneys were removed and immediately transferred to a solution of 18% sucrose and 1% PFA in phosphate buffer (0.1 M, pH 7.4). After 6 h, kidneys were washed with DPBS and cryoprotected at −80 °C until further processing. For cryosections, the organs were embedded in Tissue Tek O.C.T. Compound (Sakura Finetek, Torrance, CA, USA), cut into 5 μm sections using a CryoStar NX70 cryotome (Thermo Fisher Scientific, Waltham, MA, USA), and fixed on Superfrost plus glass slides (Thermo Fisher Scientific, Schwerte, Germany).

For analysis of NP kidney deposition and glomerular fluorescence quantification, sections were rinsed in DPBS and blocked with 5% BSA supplemented with 0.04% Triton-X in DPBS for 10 min at RT. After further rinsing in DPBS, samples were stained for cell nuclei with a 1:400 dilution of DAPI in 0.5% BSA and 0.04% Triton-X in DPBS. After the final washing step in DPBS and mpH$_2$O, cryosections were mounted with Mowiol mounting medium and analyzed on a Zeiss Axiovert 200 M.

For image analysis, Fiji software (Madison, WI, USA) was used. Glomerular fluorescence intensities were evaluated by measuring the integrated density of areas over a certain fluorescence threshold and division by the respective glomerular area.

To assess the exact cellular location of NPs, kidney cryosections were prepared as described above. After washing and blocking of sections, samples were stained overnight at 4 °C with a goat-derived integrin α-8 antibody (1:200 dilution in 0.5% BSA/0.04% Triton-X in DPBS). Samples were thereafter washed with DPBS and stained with a 1:400 dilution of Cy2 donkey anti-goat and DAPI in 0.5% BSA/0.04% Triton-X in DPBS for 1 h at RT. After the final washing step, samples were mounted and analyzed at a Zeiss LSM 710.

ASSOCIATED CONTENT

Supporting Information

The Supporting Information is available free of charge at https://pubs.acs.org/doi/10.1021/acsami.0c10057.

Further information about the concept, characterization of the polymer and particle species, and additional data of the *in vitro/in vivo* experiments (PDF)

AUTHOR INFORMATION

Corresponding Author

Achim Goepferich − *Department of Pharmaceutical Technology, University of Regensburg, 93053 Regensburg, Germany*; orcid.org/0000-0002-7646-0252; Email: Achim.Goepferich@ur.de

Authors

Daniel Fleischmann − *Department of Pharmaceutical Technology, University of Regensburg, 93053 Regensburg, Germany*

Sara Maslanka Figueroa − *Department of Pharmaceutical Technology, University of Regensburg, 93053 Regensburg, Germany*

Sebastian Beck − *Department of Pharmaceutical Technology, University of Regensburg, 93053 Regensburg, Germany*

Kathrin Abstiens − *Department of Pharmaceutical Technology, University of Regensburg, 93053 Regensburg, Germany*

Ralph Witzgall − *Institute for Molecular and Cellular Anatomy, University of Regensburg, 93053 Regensburg, Germany*

Frank Schweda − *Department of Physiology II, Institute for Physiology, University of Regensburg, 93053 Regensburg, Germany*

Philipp Tauber − *Department of Physiology II, Institute for Physiology, University of Regensburg, 93053 Regensburg, Germany*

Complete contact information is available at:
https://pubs.acs.org/10.1021/acsami.0c10057

Author Contributions

A.G. proposed the research; D.F., S.M.F., S.B., K.A., and A.G. designed the research; D.F. performed the research and analyzed the data; D.F., S.M.F., S.B., P.T., and F.S. performed the animal experiments; D.F., S.M.F., S.B., K.A., P.T., R.W., F.S., and A.G. discussed the results and commented on the manuscript; and D.F. and A.G. wrote the paper.

Notes

The authors declare no competing financial interest.

REFERENCES

(1) Wilhelm, S.; Tavares, A. J.; Dai, Q.; Ohta, S.; Audet, J.; Dvorak, H. F.; Chan, W. C. W. Analysis of Nanoparticle Delivery to Tumours. *Nat. Rev. Mater.* **2016**, *1*, 16014.

(2) Bae, Y. H.; Park, K. Targeted Drug Delivery to Tumors: Myths, Reality and Possibility. *J. Controlled Release* **2011**, *153*, 198−205.

(3) Awasthi, R.; Roseblade, A.; Hansbro, P. M.; Rathbone, M. J.; Dua, K.; Bebawy, M. Nanoparticles in Cancer Treatment:

Opportunities and Obstacles. *Curr. Drug Targets* **2018**, *19*, 1696−1709.

(4) Nel, A. E.; Mädler, L.; Velegol, D.; Xia, T.; Hoek, E. M. V.; Somasundaran, P.; Klaessig, F.; Castranova, V.; Thompson, M. Understanding Biophysicochemical Interactions at the Nano-Bio Interface. *Nat. Mater.* **2009**, *8*, 543−557.

(5) Torrice, M. Does Nanomedicine Have a Delivery Problem? *ACS Cent. Sci.* **2016**, *2*, 434−437.

(6) Ploss, A.; Evans, M. J. Hepatitis C Virus Host Cell Entry. *Curr. Opin. Virol.* **2012**, *2*, 14−19.

(7) Wilen, C. B.; Tilton, J. C.; Doms, R. W. HIV: Cell Binding and Entry. *Cold Spring Harbor Perspect. Med.* **2012**, a006866.

(8) Gagliardi, M. Biomimetic and Bioinspired Nanoparticles for Targeted Drug Delivery. *Ther. Delivery* **2017**, *8*, 289−299.

(9) Marsh, M.; Helenius, A. Virus Entry: Open Sesame. *Cell* **2006**, *124*, 729−740.

(10) Lindenbach, B. D.; Rice, C. M. The Ins and Outs of Hepatitis C Virus Entry and Assembly. *Nat. Rev. Microbiol.* **2013**, *11*, 688−700.

(11) Boulant, S.; Stanifer, M.; Lozach, P.-Y. Dynamics of Virus-Receptor Interactions in Virus Binding, Signaling, and Endocytosis. *Viruses* **2015**, *7*, 2794−2815.

(12) Grove, J.; Marsh, M. The Cell Biology of Receptor-Mediated Virus Entry. *J. Cell Biol.* **2011**, *195*, 1071−1082.

(13) Xiong, X.-B.; Uludağ, H.; Lavasanifar, A. Virus-Mimetic Polymeric Micelles for Targeted siRNA Delivery. *Biomaterials* **2010**, *31*, 5886−5893.

(14) Ni, R.; Zhou, J.; Hossain, N.; Chau, Y. Virus-Inspired Nucleic Acid Delivery System: Linking Virus and Viral Mimicry. *Adv. Drug Delivery Rev.* **2016**, *106*, 3−26.

(15) Jang, C.; Lee, J. H.; Sahu, A.; Tae, G. The Synergistic Effect of Folate and RGD Dual Ligand of Nanographene Oxide on Tumor Targeting and Photothermal Therapy In Vivo. *Nanoscale* **2015**, *7*, 18584−18594.

(16) Chu, Y.; Chen, N.; Yu, H.; Mu, H.; He, B.; Hua, H.; Wang, A.; Sun, K. Topical Ocular Delivery to Laser-Induced Choroidal Neovascularization by Dual Internalizing RGD and TAT Peptide-Modified Nanoparticles. *Int. J. Nanomed.* **2017**, *Volume 12*, 1353−1368.

(17) Li, X.; Zhou, H.; Yang, L.; Du, G.; Pai-Panandiker, A. S.; Huang, X.; Yan, B. Enhancement of Cell Recognition In Vitro by Dual-Ligand Cancer Targeting Gold Nanoparticles. *Biomaterials* **2011**, *32*, 2540−2545.

(18) Maslanka Figueroa, S.; Veser, A.; Abstiens, K.; Fleischmann, D.; Beck, S.; Goepferich, A. Influenza A Virus Mimetic Nanoparticles Trigger Selective Cell Uptake. *Proc. Natl. Acad. Sci. U. S. A.* **2019**, 9831.

(19) Maslanka Figueroa, S.; Fleischmann, D.; Beck, S.; Tauber, P.; Witzgall, R.; Schweda, F.; Goepferich, A. Nanoparticles Mimicking Viral Cell Recognition Strategies Are Superior Transporters into Mesangial Cells. *Adv. Sci.* **2020**, 1903204.

(20) Schlöndorff, D. Roles of the Mesangium in Glomerular Function. *Kidney Int.* **1996**, *49*, 1583−1585.

(21) Schlöndorff, D.; Banas, B. The Mesangial Cell Revisited: No Cell Is an Island. *J. Am. Soc. Nephrol.* **2009**, *20*, 1179−1187.

(22) Scindia, Y. M.; Deshmukh, U. S.; Bagavant, H. Mesangial Pathology in Glomerular Disease: Targets for Therapeutic Intervention. *Adv. Drug Delivery Rev.* **2010**, *62*, 1337−1343.

(23) Kolset, S. O.; Reinholt, F. P.; Jenssen, T. Diabetic Nephropathy and Extracellular Matrix. *J. Histochem. Cytochem.* **2012**, *60*, 976−986.

(24) Umanath, K.; Lewis, J. B. Update on Diabetic Nephropathy: Core Curriculum 2018. *Am. J. Kidney Dis.* **2018**, *71*, 884−895.

(25) Luisoni, S.; Greber, U. F. Biology of Adenovirus Cell Entry. In *Adenoviral vectors for gene therapy*; Academic Press, pp 27−58.

(26) Ghebremedhin, B. Human Adenovirus: Viral Pathogen with Increasing Importance. *Eur. J. Microbiol. Immunol.* **2014**, *4*, 26−33.

(27) Bewley, M. C.; Springer, K.; Zhang, Y.-B.; Freimuth, P.; Flanagan, J. M. Structural Analysis of the Mechanism of Adenovirus Binding to Its Human Cellular Receptor CAR. *Science* **1999**, *286*, 1579−1583.

(28) Burckhardt, C. J.; Suomalainen, M.; Schoenenberger, P.; Boucke, K.; Hemmi, S.; Greber, U. F. Drifting Motions of the Adenovirus Receptor CAR and Immobile Integrins Initiate Virus Uncoating and Membrane Lytic Protein Exposure. *Cell Host Microbe* **2011**, *10*, 105−117.

(29) Offringa, A.; Montijn, R.; Singh, S.; Paul, M.; Pinto, Y. M.; Pinto-Sietsma, S.-J. The Mechanistic Overview of SARS-CoV-2 Using Angiotensin-Converting Enzyme 2 to Enter the Cell for Replication: Possible Treatment Options Related to the Renin-Angiotensin System. *Eur. Heart J. Cardiovasc. Pharmacother.* **2020**, pvaa053.

(30) Abstiens, K.; Gregoritza, M.; Goepferich, A. M. Ligand Density and Linker Length are Critical Factors for Multivalent Nanoparticle-Receptor Interactions. *ACS Appl. Mater. Interfaces* **2019**, *11*, 1311−1320.

(31) Miura, S.-i.; Karnik, S. S.; Saku, K. Review: Angiotensin II Type 1 Receptor Blockers: Class Effects Versus Molecular Effects. *J. Renin Angiotensin Aldosterone Syst.* **2010**, *12*, 1−7.

(32) Yan, Y.-D.; Kim, H.-K.; Seo, K.-H.; Lee, W. S.; Lee, G.-S.; Woo, J.-S.; Yong, C.-S.; Choi, H.-G. The Physicochemical Properties, In Vitro Metabolism and Pharmacokinetics of a Novel Ester Prodrug of EXP3174. *Mol. Pharmaceutics* **2010**, *7*, 2132−2140.

(33) Zhan, C.; Gu, B.; Xie, C.; Li, J.; Liu, Y.; Lu, W. Cyclic RGD Conjugated Poly(ethylene glycol)-co-poly(lactic acid) Micelle Enhances Paclitaxel Anti-Glioblastoma Effect. *J. Controlled Release* **2010**, *143*, 136−142.

(34) Kluza, E.; van der Schaft, D. W. J.; Hautvast, P. A. I.; Mulder, W. J. M.; Mayo, K. H.; Griffioen, A. W.; Strijkers, G. J.; Nicolay, K. Synergistic Targeting of Alphavbeta3 Integrin and Galectin-1 with Heteromultivalent Paramagnetic Liposomes for Combined MR Imaging and Treatment of Angiogenesis. *Nano Lett.* **2010**, *10*, 52−58.

(35) Graf, N.; Bielenberg, D. R.; Kolishetti, N.; Muus, C.; Banyard, J.; Farokhzad, O. C.; Lippard, S. J. $\alpha(V)\beta(3)$ Integrin-Targeted PLGA-PEG Nanoparticles for Enhanced Anti-Tumor Efficacy of a Pt(IV) Prodrug. *ACS Nano* **2012**, *6*, 4530−4539.

(36) Wilder, R. L. Integrin Alpha V Beta 3 as a Target for Treatment of Rheumatoid Arthritis and Related Rheumatic Diseases. *Ann. Rheum. Dis.* **2002**, *61*, ii96.

(37) Abstiens, K.; Maslanka Figueroa, S.; Gregoritza, M.; Goepferich, A. M. Interaction of Functionalized Nanoparticles with Serum Proteins and its Impact on Colloidal Stability and Cargo Leaching. *Soft Matter* **2019**, *15*, 709−720.

(38) Moghimi, S. M.; Hunter, A. C.; Andresen, T. L. Factors Controlling Nanoparticle Pharmacokinetics: An Integrated Analysis and Perspective. *Annu. Rev. Pharmacol. Toxicol.* **2012**, *52*, 481−503.

(39) Aggarwal, P.; Hall, J. B.; McLeland, C. B.; Dobrovolskaia, M. A.; McNeil, S. E. Nanoparticle Interaction with Plasma Proteins as it Relates to Particle Biodistribution, Biocompatibility and Therapeutic Efficacy. *Adv. Drug Delivery Rev.* **2009**, *61*, 428−437.

(40) Makadia, H. K.; Siegel, S. J. Poly Lactic-co-Glycolic Acid (PLGA) as Biodegradable Controlled Drug Delivery Carrier. *Polymer* **2011**, *3*, 1377−1397.

(41) Abstiens, K.; Fleischmann, D.; Gregoritza, M.; Goepferich, A. M. Gold-Tagged Polymeric Nanoparticles with Spatially Controlled Composition for Enhanced Detectability in Biological Environments. *ACS Appl. Nano Mater.* **2019**, *2*, 917−926.

(42) Xiao, R. Z.; Zeng, Z. W.; Zhou, G. L.; Wang, J. J.; Li, F. Z.; Wang, A. M. Recent Advances in PEG-PLA Block Copolymer Nanoparticles. *Int. J. Nanomed.* **2010**, *5*, 1057−1065.

(43) Qian, H.; Wohl, A. R.; Crow, J. T.; Macosko, C. W.; Hoye, T. R. A Strategy for Control of ″Random″ Copolymerization of Lactide and Glycolide: Application to Synthesis of PEG-b-PLGA Block Polymers Having Narrow Dispersity. *Macromolecules* **2011**, *44*, 7132−7140.

(44) Satchell, S. C.; Braet, F. Glomerular Endothelial Cell Fenestrations: an Integral Component of the Glomerular Filtration Barrier. *Am. J. Physiol. Renal Physiol.* **2009**, *296*, F947−F956.

(45) Latta, H. An Approach to the Structure and Function of the Glomerular Mesangium. *J. Am. Soc. Nephrol.* **1992**, *2*, S65−S73.

(46) He, C.; Hu, Y.; Yin, L.; Tang, C.; Yin, C. Effects of Particle Size and Surface Charge on Cellular Uptake and Biodistribution of Polymeric Nanoparticles. *Biomaterials* **2010**, *31*, 3657−3666.

(47) Hennig, R.; Ohlmann, A.; Staffel, J.; Pollinger, K.; Haunberger, A.; Breunig, M.; Schweda, F.; Tamm, E. R.; Goepferich, A. Multivalent Nanoparticles Bind the Retinal and Choroidal Vasculature. *J. Controlled release : Official J. Controlled Release Soc.* **2015**, *220*, 265−274.

(48) Pollinger, K.; Hennig, R.; Breunig, M.; Tessmar, J.; Ohlmann, A.; Tamm, E. R.; Witzgall, R.; Goepferich, A. Kidney Podocytes as Specific Targets for Cyclo(RGDfC)-Modified Nanoparticles. *Small* **2012**, *8*, 3368−3375.

(49) Hennig, R.; Pollinger, K.; Veser, A.; Breunig, M.; Goepferich, A. Nanoparticle Multivalency Counterbalances the Ligand Affinity Loss upon PEGylation. *J. Controlled Release* **2014**, *194*, 20−27.

(50) Doherty, G. J.; McMahon, H. T. Mechanisms of Endocytosis. *Annu. Rev. Biochem.* **2009**, *78*, 857−902.

(51) Liu, M.; Li, Q.; Liang, L.; Li, J.; Wang, K.; Li, J.; Lv, M.; Chen, N.; Song, H.; Lee, J.; Shi, J.; Wang, L.; Lal, R.; Fan, C. Real-Time Visualization of Clustering and Intracellular Transport of Gold Nanoparticles by Correlative Imaging. *Nat. Commun.* **2017**, *8*, 15646.

(52) Sahay, G.; Alakhova, D. Y.; Kabanov, A. V. Endocytosis of Nanomedicines. *J. Controlled Release : Official J. Controlled Release Soc.* **2010**, *145*, 182−195.

(53) Cai, W.; Gao, T.; Hong, H.; Sun, J. Applications of Gold Nanoparticles in Cancer Nanotechnology. *Nanotechnol. Sci. Appl.* **2008**, *Volume 1*, 17−32.

(54) Llevot, A.; Astruc, D. Applications of Vectorized Gold Nanoparticles to the Diagnosis and Therapy of Cancer. *Chem. Soc. Rev.* **2012**, *41*, 242−257.

(55) Sperling, R. A.; Rivera Gil, P.; Zhang, F.; Zanella, M.; Parak, W. J. Biological Applications of Gold Nanoparticles. *Chem. Soc. Rev.* **2008**, *37*, 1896−1908.

(56) Blanco, E.; Shen, H.; Ferrari, M. Principles of Nanoparticle Design for Overcoming Biological Barriers to Drug Delivery. *Nat. Biotechnol.* **2015**, *33*, 941−951.

(57) Hodivala-Dilke, K. $\alpha v \beta 3$ Integrin and Angiogenesis: a Moody Integrin in a Changing Environment. *Curr. Opin. Cell Biol.* **2008**, *20*, 514−519.

(58) Figueroa, S. M.; Fleischmann, D.; Beck, S.; Goepferich, A. Thermodynamic, Spatial and Methodological Considerations for the Manufacturing of Therapeutic Polymer Nanoparticles. *Pharm. Res.* **2020**, *37*, 59.

(59) Valencia, P. M.; Hanewich-Hollatz, M. H.; Gao, W.; Karim, F.; Langer, R.; Karnik, R.; Farokhzad, O. C. Effects of Ligands with Different Water Solubilities on Self-assembly and Properties of Targeted Nanoparticles. *Biomaterials* **2011**, *32*, 6226−6233.

(60) Childs, C. E. The Determination of Polyethylene Glycol in Gamma Globulin Solutions. *Microchem. J.* **1975**, *20*, 190−192.

(61) Rabanel, J.-M.; Faivre, J.; Tehrani, S. F.; Lalloz, A.; Hildgen, P.; Banquy, X. Effect of the Polymer Architecture on the Structural and Biophysical Properties of PEG-PLA Nanoparticles. *ACS Appl. Mater. Interfaces* **2015**, *7*, 10374−10385.

(62) Grynkiewicz, G.; Poenie, M.; Tsien, R. Y. A New Generation of Ca2+ Indicators with Greatly Improved Fluorescence Properties. *J. Biol. Chem.* **1985**, *260*, 3440−3450.